IOP Publishing | Royal Swedish Academy of Sciences Physica Scripta

Phys. Scr. T169 (2016) 014002 (15pp) doi:10.1088/0031-8949/T169/1/014002

Multidimensional resonant nonlinear spectroscopy with coherent broadband x-ray pulses

Kochise Bennett[1,2], **Yu Zhang**[1], **Markus Kowalewski**[1], **Weijie Hua**[1,3] and **Shaul Mukamel**[1,2,4,5]

[1] Department of Chemistry, University of California, Irvine, CA 92697-2025
[2] The Department of Physics and Astronomy, University of California, Irvine, CA 92697-4575
[3] Department of Theoretical Chemistry and Biology, School of Biotechnology, KTH Royal Institute of Technology, S-10691 Stockholm, Sweden
[4] The Freiburg Institute for Advanced Studies (FRIAS)

E-mail: kcbennet@uci.edu, yuz10@uci.edu, mkowalew@uci.edu, hua@theochem.kth.se and smukamel@uci.edu

Received 12 November 2015, revised 10 March 2016
Accepted for publication 14 March 2016
Published 16 June 2016

Abstract

New x-ray free electron laser (XFEL) and high harmonic generation (HHG) light sources are capable of generating short and intense pulses that make x-ray nonlinear spectroscopy possible. Multidimensional spectroscopic techniques, which have long been used in the nuclear magnetic resonance, infrared, and optical regimes to probe the electronic structure and nuclear dynamics of molecules by sequences of short pulses with variable delays, can thus be extended to the attosecond x-ray regime. This opens up the possibility of probing core-electronic structure and couplings, the real-time tracking of impulsively created valence-electronic wavepackets and electronic coherences, and monitoring ultrafast processes such as nonadiabatic electron-nuclear dynamics near conical-intersection crossings. We survey various possible types of multidimensional x-ray spectroscopy techniques and demonstrate the novel information they can provide about molecules.

Keywords: x-ray, spectroscopy, Raman, four-wave-mixing

(Some figures may appear in colour only in the online journal)

1. Introduction

A major motivation for developing x-ray free-electron lasers (XFELs) has been the diffraction off nanocrystals or even single-molecule samples. Such experiments provide ultrafast, stroboscopic snapshots of the evolving electron charge density, resulting in real-time movies of structural changes without the need for crystalization. This could revolutionize the study of structural dynamics of chemical reactions and biological processes [1, 2]. In this article, we survey a different class of techniques that are made possible by these novel light sources. These involve detecting the ultrafast response of matter to sequences of x-ray pulses which are resonant with core transitions in selected atoms. These are natural extensions of multidimensional techniques first developed in nuclear magnetic resonance (NMR) and gradually extended to higher frequency regimes [3, 4].

Linear spectroscopy signals are recorded versus a single time or frequency parameter, revealing one-dimensional (1D) information on energy levels, transition dipole moments, and electronic and nuclear motions in molecules. Multidimensional spectroscopy uses sequences of laser pulses to perturb the system and probe correlated events taking place during well-controlled time intervals. These nonlinear techniques ultimately reveal multipoint correlation functions of matter which carry significantly more detailed dynamical information than the two-point correlation functions

---

[5] Author to whom any correspondence should be addressed.

0031-8949/16/014002+15$33.00

corresponding to 1D techniques [5]. For example, 2D spectroscopy has long been used in the NMR/radiowave regime to reveal couplings between nuclear spins [6]. Signals are displayed versus two frequency axes. Excitation energies appear along the diagonal and the diagonal slice of this plot therefore corresponds to ordinary 1D spectroscopy. Off-diagonal cross peaks on the 2D spectrum reveal couplings/interactions between the various excitations of the system. Multidimensional NMR is commonly used to determine the fluctuating conformations of complex biomolecular systems with high structural resolution [7]. The past two decades have seen these concepts extended to the infrared (IR) and optical regimes, where new degrees of freedom other than nuclear spins are probed and enhanced temporal resolution (from the millisecond to the femtosecond regime) is possible [4, 8]. Multidimensional techniques are particularly useful for systems with congested 1D spectra or to probe transient properties of the perturbed system, and can reveal excitation correlations and other many-body effects [9]. 2D optical Raman and 2D IR has now been used to obtain important structural and dynamical information that was not accessible with conventional 1D optical techniques [10, 11]. At present, the technology exists for 2D UV and extreme ultraviolet (XUV) spectroscopy and attosecond x-ray pulses extend it for core excitations [12–14].

X-ray pulses can resonantly excite core electrons. 1D techniques, such as x-ray absorption near-edge structure (XANES), reveal the core excitations and the valence fine structure. This is in analogy to how optical absorption reveals valence electronic excitation and vibrational substructure. 2D x-ray spectroscopy may be used to investigate the interactions between core excitations. Since core energy levels are highly element-specific, this can be used to probe structural and dynamic information in complicated molecules with high spatial resolution. The broad bandwidth of x-ray pulses makes it possible to probe many states on a very short timescale [15].

Many important processes are ill-understood because they are too fast to be probed with femtosecond-to-picosecond techniques or require a broader spectral width than optical pulses allow. Ultrafast processes such as intersystem crossing, radiationless decay, passage through conical intersections, and the dynamics and effects of electronic coherence are ubiquitous in nature [16] but have evaded complete understanding due to the extreme temporal and spectral parameter regimes necessary for their observation. Tunable intense attosecond x-ray pulses can probe such ultrafast processes and so gain a greater comprehension of the physics and chemistry that underlies a broad array of material phenomena [17, 18]. Coherent x-ray pulses as short as 35 as have been produced via high-harmonic generation [19–21]. These pulses are easier to generate and of much higher quality than XFEL pulses but they are of significantly lower intensity, which makes it harder to use them in higher-order nonlinear spectroscopies. In this article, we provide a broad perspective on recent work combining these exciting new pulse regimes with the aforementioned multidimensional spectroscopies as well as presenting new calculations in section 2.

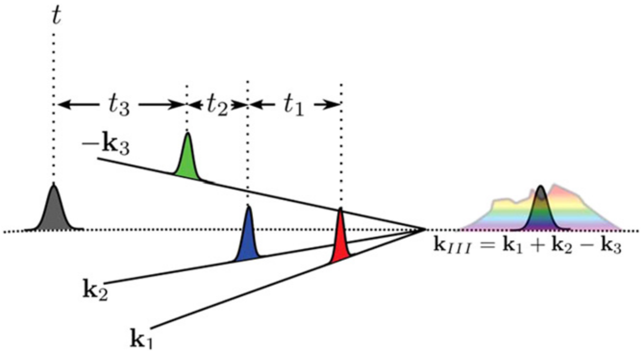

Figure 1. Schematic sketch of an FWM experiment. The figure depicts the $\mathbf{k}_{\rm III} = \mathbf{k}_1 + \mathbf{k}_2 - \mathbf{k}_3$ DQC signal. This and the signal $\mathbf{k}_{\rm I} = -\mathbf{k}_1 + \mathbf{k}_2 + \mathbf{k}_3$ (photon echo) are discussed in the text. Figure adapted and reproduced with permission from [27]. Copyright AIP Publishing 2013.

2. Four-wave mixing: the double quantum coherence signal

Four-wave mixing (FWM) is the most common type of nonlinear spectroscopic technique. In this experiment (figure 1), a sequence of three pulses interacts with the material under study to generate a signal which is detected along one of the linear combinations of the three incoming pulse directions. Based on phase-matching, there are four independent possible signals $\mathbf{k}_{\rm I} = -\mathbf{k}_1 + \mathbf{k}_2 + \mathbf{k}_3$, $\mathbf{k}_{\rm II} = +\mathbf{k}_1 - \mathbf{k}_2 + \mathbf{k}_3$, $\mathbf{k}_{\rm III} = +\mathbf{k}_1 + \mathbf{k}_2 - \mathbf{k}_3$, and $\mathbf{k}_{\rm IV} = +\mathbf{k}_1 + \mathbf{k}_2 + \mathbf{k}_3$. We shall primarily discuss the $\mathbf{k}_{\rm I}$ and $\mathbf{k}_{\rm III}$ techniques. The signal intensity can be detected either directly (homodyne detection) or by interference with a fourth local oscillator pulse along the detected direction (heterodyne detection). The latter is experimentally more challenging, since it requires a phase-sensitive detection, but yields additional information about the matter response and a stronger signal amplified by the strong detection pulse. Careful geometric phase-matching must be done to separate the various signals. The same information can be alternatively obtained in a colinear geometry with phase-cycling of the interacting fields (i.e. combining the results of repeated measurements with different pulse phase configurations) [22, 23].

FWM signals are related to a four-point correlation function of the dipole operator, which is a function of the three time delays (t_j) as well as other pulse parameters such as the frequencies (ω_j). Since the system interacts with each pulse in sequence, varying the pulse parameters and delays allows one to control the generation and evolution of excited states and coherences. Compared to linear 1D signals, FWM 3D experiments are rich with information on multiply excited states and their dynamics but are more difficult to measure, being of a higher interaction order and requiring higher intensities and phase-matching to separate the signals for interpretation (we note that '2D' and '3D' FWM involve the same experimental setup with the former signal being 2D slices of the latter and thus easier to display). The extension of

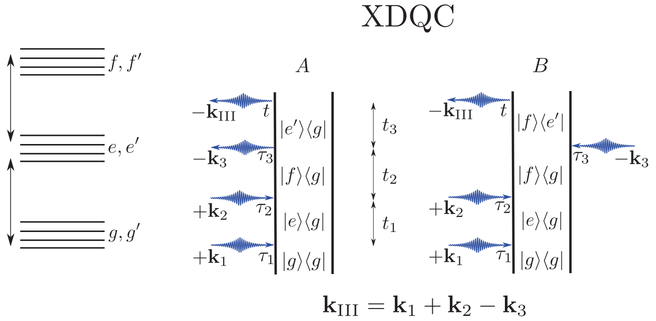

Figure 2. Left: level scheme for core FWM spectroscopy, where gg', ee', ff' represent states with 0, 1, and 2 core excitations, respectively. Each manifold's substructure stands for valence excitations and the arrows represent transition dipoles. Right: ladder diagrams fo XDQC. FWM techniques require full time-ordering which is maintained by the ladder diagrams. For diagram rules, see [28].

FWM techniques to the x-ray regime has been discussed and realized recently in the XUV [14, 24–26]. Below, we present one FWM signal in detail.

Double-quantum coherence (DQC) is the name given to the FWM signal generated at $\mathbf{k}_{\rm III} = \mathbf{k}_1 + \mathbf{k}_2 - \mathbf{k}_3$. The signal is represented by the two diagrams shown in figure 2, both of which promote the molecular density matrix, via interaction with the first two pulses, to a double-core-excited state coherence $\rho_{gg} \mapsto \rho_{eg} \mapsto \rho_{fg}$. The third interaction leaves the system in either of two coherences, ρ_{fe} or ρ_{eg} for the final propagation period (we make the rotating wave approximation (RWA) whereby field and matter frequencies are of opposite sign for each field–matter interaction). One important property of DQC is that these two diagrams exactly cancel each other when the system is harmonic (so that $\omega_{eg} = \omega_{fe}$). This is possible when the double core-hole (DCH) is created on two weakly coupled atoms of the same element. Thus, this signal offers a background-free detection of anharmonicities in the energy eigenbasis of the system. In excitonic systems, the anharmonicities stem from interactions betwen excitonic quasiparticles (deviations from bosonic behavior) and DQC can be used to probe the exciton–exciton coupling in chromophore aggregates, semiconductor quantum wells, etc [29]. In the x-ray regime (x-ray DQC or XDQC), this technique reveals coupling between core excitations [27, 30]. Since these excitations are generally well-localized and element-specific, this technique provides detailed information on core-excitation dynamics and many-body interactions. XDQC and the other XFWM signals were discussed for various models of multiple core-hole coherence [26]. The $\mathbf{k}_{\rm III}$ signal is given by [31, 32]

$$S_{\rm III}(\Omega_3, \Omega_2, \Omega_1) = S_{\rm III,A}(\Omega_3, \Omega_2, \Omega_1) + S_{\rm III,B}(\Omega_3, \Omega_2, \Omega_1), \tag{1}$$

where

$$\begin{aligned} S_{\rm III,A}(\Omega_3, \Omega_2, \Omega_1) = &\sum_{fe'e} \mathcal{E}_4^*(\omega_4 - \omega_{e'g})\mathcal{E}_3^*(\omega_3 - \omega_{fe'}) \\ &\times \mathcal{E}_2(\omega_2 - \omega_{fe})\mathcal{E}_1(\omega_1 - \omega_{eg}) \frac{\mathbf{V}_{ge'} \cdot \mathbf{e}_4}{(\Omega_3 - \omega_{e'g} + i\gamma_{e'g})} \\ &\times \frac{(\mathbf{V}_{e'f} \cdot \mathbf{e}_3)(\mathbf{V}_{fe} \cdot \mathbf{e}_2)}{(\Omega_2 - \omega_{fg} + i\gamma_{fg})} \frac{\mathbf{V}_{eg} \cdot \mathbf{e}_1}{(\Omega_1 - \omega_{eg} + i\gamma_{eg})}, \end{aligned} \tag{2}$$

$$\begin{aligned} S_{\rm III,B}(\Omega_3, \Omega_2, \Omega_1) = -&\sum_{fe'e} \mathcal{E}_4^*(\omega_4 - \omega_{fe'})\mathcal{E}_3^*(\omega_3 - \omega_{e'g}) \\ &\times \mathcal{E}_2(\omega_2 - \omega_{fe})\mathcal{E}_1(\omega_1 - \omega_{eg}) \frac{\mathbf{V}_{e'f} \cdot \mathbf{e}_4}{(\Omega_3 - \omega_{fe'} + i\gamma_{fe'})} \\ &\times \frac{(\mathbf{V}_{ge'} \cdot \mathbf{e}_3)(\mathbf{V}_{fe} \cdot \mathbf{e}_2)}{(\Omega_2 - \omega_{fg} + i\gamma_{fg})} \frac{\mathbf{V}_{eg} \cdot \mathbf{e}_1}{(\Omega_1 - \omega_{eg} + i\gamma_{eg})}. \end{aligned} \tag{3}$$

Here $S_{\rm III,A}$ and $S_{\rm III,B}$ refer to the two diagrams in figure 2 with Ω_j the Fourier conjugate to the delay time t_j. $\mathcal{E}_j$ and $\mathbf{e}_j$ are the pulse spectral envelope and polarization vector of the jth pulse while the $\mathbf{V}$'s denote the transition dipole moments. g is the ground state, and e/e' and f denote the single (SCH) and double core-hole excited states, respectively. γ_α is the lifetime broadening of state α with $\gamma_{\alpha\beta} = \gamma_\alpha + \gamma_\beta$, and $\omega_{\alpha\beta} = \omega(\alpha) - \omega(\beta)$ stands for the transition energy.

Figure 3 presents the simulated XANES spectra and XDQC signals of three isomers of aminophenols, which have a –NH$_2$ and a –OH group bonded to benzene with para-, meta-, and ortho- positions (abbreviated as p-, m-, o-, respectively) [33]. Calculations were performed at the state-averaged restricted active space self-consistent field (SA-RASSCF) [34] level, which adequately considers the static correlation and orbital relaxation caused by core holes. Nonlinear x-ray spectroscopy poses new computational challenges for core excitations (see [35] for a review on different methods). RASSCF can treat the valence, SCH and DCH states at the same level, which gets a balanced accuracy for their couplings and the signals. The method was first employed in core-hole calculations in the 1980s [36–39], and recently used to calculate double ionized states and spectra of small molecules [40], L-edge XANES and resonant inelastic x-ray scattering (RIXS) spectra of transition metal complexes [41], and linear and nonlinear x-ray spectra of conical intersection structures [42]. In figure 3(a), isomers show similar XANES spectra at both the N and O K-edges which would require high-resolution measurement to detect and distinguish the fine structures. The XDQC signals show higher sensitivity, see Ω_1–Ω_2 and Ω_3–Ω_2 correlation plots depicted in figures 3(b)–(c). Gaussian pulses with standard deviation $\sigma_j = 100$ as were used which cover an energy bandwidth of ca. 11 eV (power spectrum FWHM). We tuned the central carrier frequencies of the first two pulses at $\omega_1 = 536$ eV and $\omega_2 = 400$ eV to generate the O1s SCH excited states first and then to reach the O1sN1s intermediate DCH excited states. The frequencies were set to match $g \rightarrow e^O$ and $e^O \rightarrow f^{\rm ON}$ resonances, respectively. We set ω_3 and ω_4 at 403 eV and

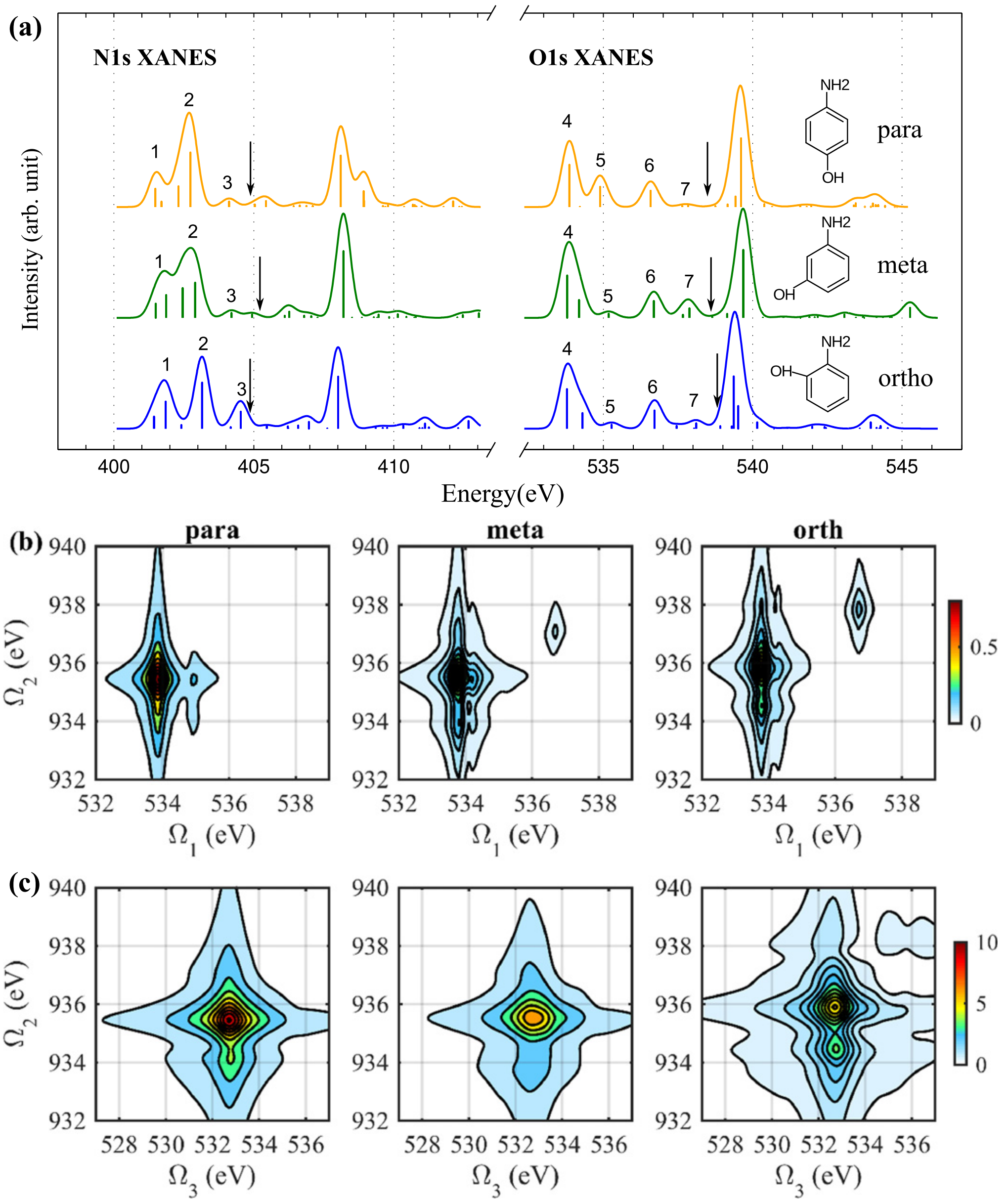

Figure 3. (a) N1s and O1s XANES spectra of p-, m-, o-aminophenols simulated by the RASSCF method. Arrows stand for the ionic potentials (IPs) calculated by the ΔKohn–Sham approach. Only bound states below IPs were used in signal calculations. Major peaks are labeled. (b), (c) Simulated XDQC signals (absolute values) at the ON-B pulse configuration: (b) $S_{\rm III}(t_3 = 6.1\ \text{fs}, \Omega_2, \Omega_1)$; (c) $S_{\rm III}(\Omega_3, \Omega_2, t_1 = 0\ \text{fs})$. Ω_1 and Ω_2 correspond respectively to O1s SCH to O1sN1s DCH states resonances (from the ground state). Ω_3 corresponds to the O1s SCH to O1sN1s DCH resonances. Pulse parameters used: $\omega_1 = 536$ eV, $\omega_2 = 400$ eV, $\omega_3 = 403$ eV, $\omega_4 = 533$ eV. All pulse durations were set $\sigma_j = 100$ as. Adapted and reproduced from [33]. Copyright Royal Society of Chemistry 2016.

533 eV, respectively tuned to match $\omega(e^N) - \omega(g)$ and $\omega(f^{\rm ON}) - \omega(e^N)$ transition energies which selects only the diagram B pathway (see equation (3)). This pulse configuration is denoted as ON-B. One diagram pathway is activated owing to the well separation of the N1s and O1s energies (~130 eV) as compared to the pulse bandwidth. The N1s and O1s orbitals in aminophenols are weakly coupled, so energies of the N1sO1s DCH states are very close to summation of the corresponding SCH state energies. In figure 3(b), the strongest peak appears at $\Omega_1 = 534$ eV in all isomers, corresponding to the O1s → $\sigma^*_{\rm OH}$ transitions in XANES (peak 4). Para-aminophenol shows a well-separated shoulder structure at $\Omega_1 = 535$ eV, which corresponds to the O1s → π^* peak in XANES (peak 5). This feature is hardly seen in the other two structures, consistent with their much weaker peak 5 intensities in XANES. It is clear that the para isomer has more stable resonance structures or more delocalized π electrons. This feature reflects the coupling of the two groups through the π^* orbitals. The diffused patterns of meta and ortho isomers in this region are related to their broader and unsymmetric XANES peak 4. Another distinguishing peak is at $\Omega_1 = 536.7$ eV, which becomes stronger as we move from p-,

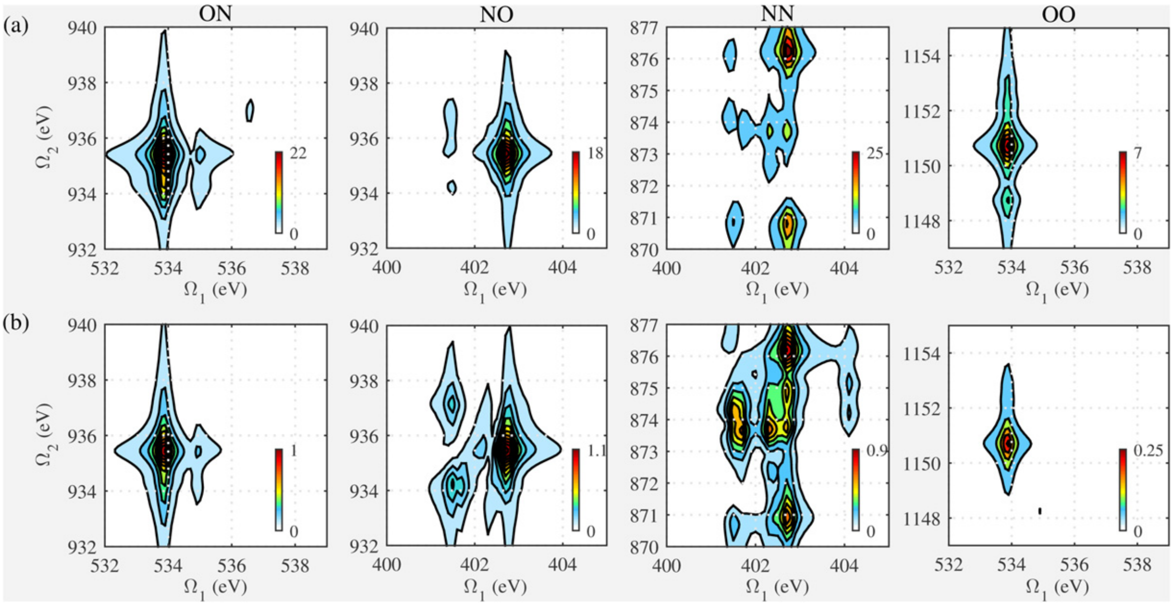

Figure 4. Simulated XDQC signals $S_{\mathrm{III}}(t_3 = 6.1\ \mathrm{fs}, \Omega_2, \Omega_1)$ (absolute values) of p-aminophenol at eight pulse configurations. ON, NO, NN, and OO denote different pulse frequencies of ω_1 and ω_2. The ON and NO setup creates two-site N1sO1s DCH excited states (initiated with O1s and N1s SCH excited states, respectively); and the NN and OO setup excites single-site N1sN1s and O1sO1s DCH states, respectively. Different ω_3 and ω_4 frequencies select either the (a) $S_{\mathrm{III,A}}$ or (b) $S_{\mathrm{III,B}}$ pathway. The eight pulse configurations are denoted for example as ON-A. Signals were simulated at the RASSCF level. All pulse durations were set $\sigma_j = 100$ as. Adapted and reproduced with permission from [33]. Copyright Royal Society of Chemistry 2016.

m-, to o-aminophenols. In the XANES spectra, the three isomers show a peak with virtually the same intensity (peak 6). This illustrates the ability of XDQC to amplify small differences in XANES. The Ω_3–Ω_2 correlation plots in figure 3(c) also show distinct patterns for different isomers. The XDQC signals are very sensitive to the small chemical structure changes around the core holes, and can see their couplings. Since core excited states are localized, the spatial correlation information inside a molecule is revealed. In conjunction with high temporal resolution, the ultrafast electron dynamics can be detected following the changes in correlation. Our example aminophenols have two electron donating groups. When one group is changed to be an electron acceptor, the molecule becomes so-called push-pull chromophores [43–46]. XDQC has the potential to see the atomic nature of the intramolecular charge transfer by creating a two-site double core on both side groups.

We next demonstrate the capacity of the XDQC technique to select different DCH pathways by tuning the pulse frequencies. RASSCF can treat different types of DCHs, located on one site (N1sN1s and O1sO1s DCHs on the –NH_2 and –OH groups) or two sites (N1sO1s DCHs). In figure 4, we show the simulated XDQC signals of p-aminophenol at eight pulse configurations (Ω_1–Ω_2 plot). Based on the excitation sequences of the first two pulses (ω_1, ω_2), we classified them as ON, NO, NN, and OO pulse configurations. The NO configuration prepares the system with N1s core excitations and then reaches two-site DCH states on both N and O atoms. The NN and OO configurations lead to single-site DCH states initiated respectively by N1s and O1s SCH excitations. By tuning the last two pulses, one can select diagram A or B. It should be noted that for single-site DCH states, the energies are not simply twice the SCH energies, but ~60 eV (~80 eV) higher for NN (OO) DCH states from our RASSCF calculations. These differences stem from the correlation of the two 1s electrons in the same shell. ω_1 and ω_2 strongly affect the energy region and patterns of the signals. Selecting diagram A or B (by tuning ω_3 and ω_4) does not affect the signal in this case.

Another FWM technique is photon echo spectroscopy (PES). This is an extension of the NMR spin echo technique in which inhomogeneous broadening is eliminated. The photon echo signal is generated in the direction $\mathbf{k}_{\mathrm{I}} = -\mathbf{k}_1 + \mathbf{k}_2 + \mathbf{k}_3$ (the corresponding ladder diagrams are given in figure 5). The first pulse excites the system from the ground state, creating an electronic coherence (the density matrix is taken from $\rho_{gg} \mapsto \rho_{eg}$, for example). After evolving in this coherence for the first time delay t_1, the system interacts with the second pulse and is left in a population (ρ_{gg} or ρ_{ee}) for the t_2 period. The third pulse brings the system back to an electronic coherence and the third propagation period t_3 begins rephasing the signal (i.e. the dephasing caused by the t_1 propagation is cancelled by the t_3 propagation). This re-phasing is complete when $t_1 = t_3$ and an echo is produced at this time. This signal can then be studied by Ω_1/Ω_3 correlation plots while varying t_2 to track changes in the echo due to the dynamics in this intermediate period. In this way, PES can be used to monitor, e.g. excitation energy transfer and charge separation in bacterial reaction centers [47]. X-ray PES will extend these studies to core electron levels, including their dephasing properties and core-hole dynamics [48–51]. We had previously calculated the photon echo signals of aminophenols [48] with the equivalent core-hole (ECH) approximation (also known as the (Z+1)

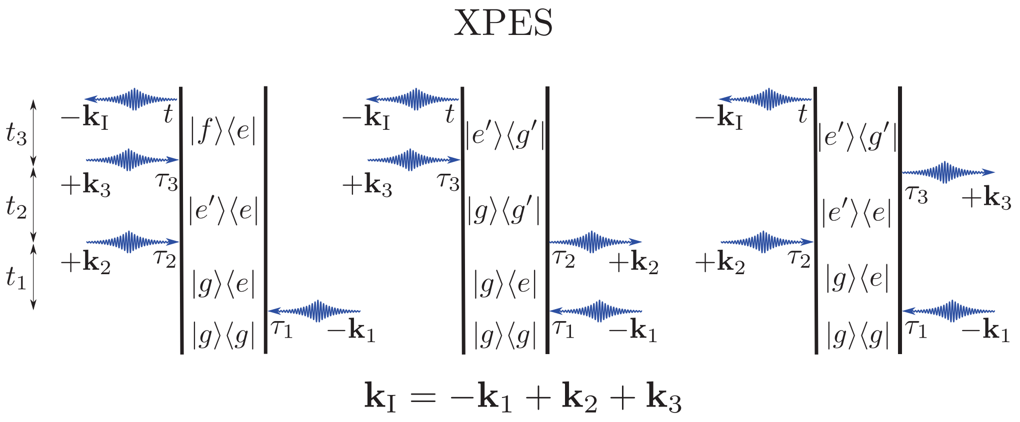

Figure 5. The three ladder diagrams for the $\mathbf{k}_I = -\mathbf{k}_1 + \mathbf{k}_2 + \mathbf{k}_3$ XPES signal. For level scheme, see figure 2.

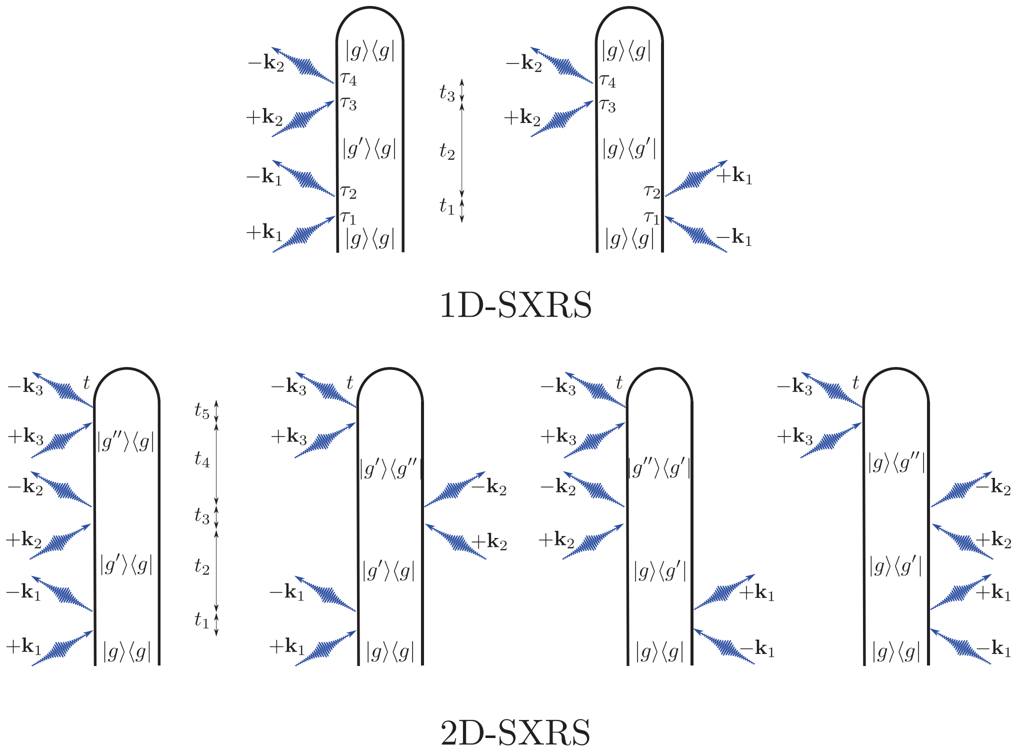

Figure 6. Loop diagrams for 1D-SXRS (top) and 2D-SXRS (bottom). These differ from the ladder diagrams of figures 2 and 5 in that the relative time-ordering of interactions on the ket and the bra are not maintained. To emphasize the Raman-style nature of the interactions, we compress the distance between pulses associated with a given excitation/deexcitation event and therefore illustrate the pulses at an angle rather than horizontally to avoid crowding. That the diagrams are topped with a loop indicates that the relative time-ordering between bra and ket interactions is not maintained, in contrast with the ladder diagrams which maintain full time-ordering. For diagram rules, see [28].

approximation) [52, 53]. In that approximation, a single core hole is represented by an additional one nuclear charge, and double core holes are represented by additional two nuclear charges, and so on. This method is very simple to apply and works for deep core holes. The simulations of figures 3 and 4 use the more accurate RASSCF.

3. Stimulated x-ray Raman signals

So far we have described XFWM techniques that probe core excitations directly. These are highly demanding experimentally, since the time observation window is limited by the core lifetimes (tens to ~1 fs) and require a complete phase control of the pulse. Stimulated x-ray Raman spectroscopy (SXRS) techniques (figure 6), in contrast, use the core states as a fast trigger of valence excitations [54]. This is analogous to the way optical pulses use intermediate electronic excitations to impulsively trigger vibrational motions, as depicted in figure 7. Since valence (e.g. $|g'\rangle\langle g|$) rather than core excitations exist during the delay periods, the short core lifetime is no longer a limitation on the time window. It is possible to perform the experiment so that the molecule interacts twice with each applied pulse so as to

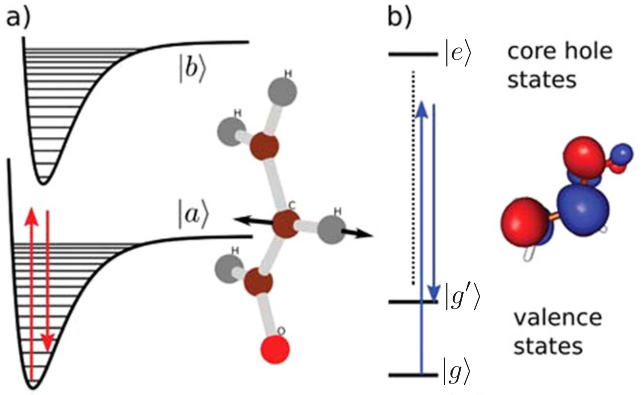

Figure 7. Vibrational (optical) Raman spectroscopy versus electronic (x-ray) Raman spectroscopy. (a) Optical Raman spectroscopy probes transitions between vibrational states. Low lying electronic valence states serve as intermediates. (b) In an x-ray Raman process, the core-hole states serve as intermediate states to induce transitions between valence electronic states.

cancel the field phases. Thus, phase control is not needed, making SXRS experimentally less challenging than the FWM techniques described above. Finally, SXRS reveals information about valence electrons, which are more chemically relevant than the core electrons which are typically frozen during chemical reactions.

The Raman excitation is cleanly encapsulated by the effective polarizability (see figure 7)

$$\alpha_{j,g'g''} = \sum_e \int d\omega \frac{\mathcal{E}_j^*(\omega)\mathcal{E}_j(\omega + \omega_{g'g''})}{\omega + \omega_j - \omega_{eg'} + i\gamma_e} \frac{V_{g'e}V_{eg''}}{2\pi}, \qquad (4)$$

where $\mathcal{E}_j$ is the spectral envelope of the jth pulse (centered at zero frequency) and ω_j is its carrier frequency [15, 55]. This is the relevant transition operator that controls core-mediated x-ray Raman valence excitations. The spectrum of the pulse can be used to control which intermediate core-excitation e is used in the Raman process and which valence states g' are accessible. Each Raman-type field–molecule interaction multiplies the wavefunction by $\hat{\alpha}$. We use the amino acid cysteine to illustrate how a stimulated resonant x-ray Raman process can create excitations localized at different target atoms in the molecule (N, O, and S). As shown in figure 8, a broadband x-ray pulse can create a valence excited state wavepacket localized to the target atoms. At time zero, all electron and hole densities are localized to the selected excited atom (figure 8(a)). We divided the molecule into three spatial regions surrounding the different functional groups (the carboxyl, the amine, and the thiol) as shown in figure 8(b). Electron and hole densities projected to these three regions at later times are presented in figure 8(c). We find that the localized nature of electrons and holes persists with some fluctuations, and usually the hole is more localized than the electron.

The various Raman techniques are given by combinations of correlations functions of $\hat{\alpha}$. For example, the 1D-SXRS signal is given by

$$S_{\mathrm{SXRS}}(t) = \Re[\langle \hat{\alpha}_{\mathrm{s}}(t)\hat{\alpha}_{\mathrm{p}}(0)\rangle - \langle \hat{\alpha}_{\mathrm{p}}^{\dagger}(0)\hat{\alpha}_{\mathrm{s}}(t)\rangle] \qquad (5)$$

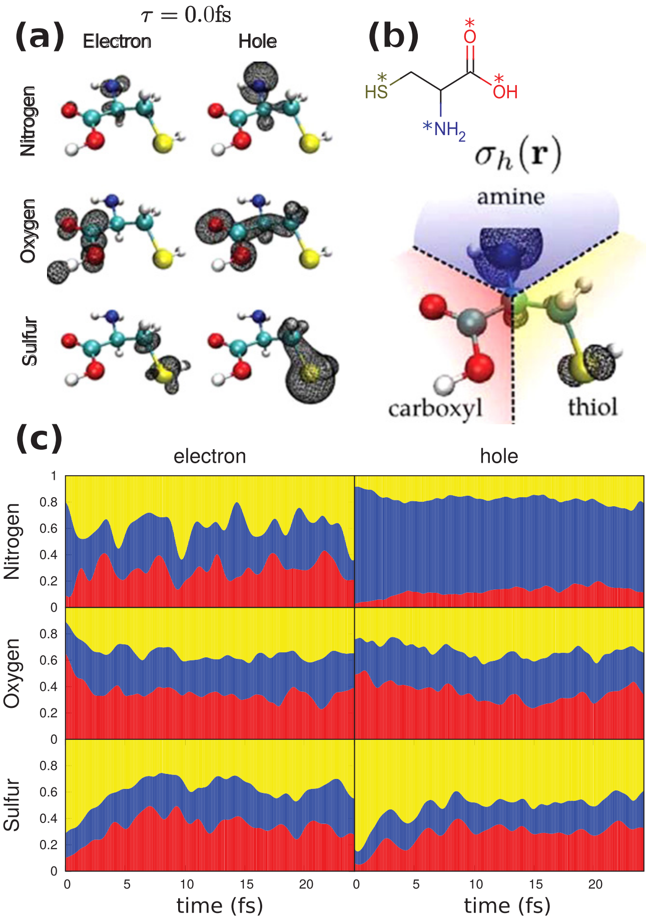

Figure 8. The localized excited state wavepacket created through stimulated x-ray Raman processes in the amino acid cysteine. (a) Reduced electron and hole density contours for the wavepackets directly after ($\tau = 0$ fs) excitations with pulses tuned to the nitrogen (top), oxygen (middle), and sulfur (bottom) K-edges. (b) Regimes of the three functional groups -NH$_2$, -COOH, and -SH. (c) Distribution of the reduced electron (left column) and hole (right) densities over the carboxyl (red), amine (blue), and thiol (yellow) functional groups after excitation with x-ray pulses tuned to the nitrogen (top row), oxygen (middle), and sulfur (bottom) K-edges. Adapted and reproduced with permission from [56]. Copyright ACS Publications 2012.

where $\Re$ denotes the real part, the subscripts p and s stand for ‘pump’ and ‘signal’, respectively, and the operator time-dependence is in the interaction picture. A broadband x-ray pulse can create a wavepacket of electronic coherences $\rho_{g'g}$ (where g' are valence-level substructure to core excitations in analogy with vibrational substructure of valence excitations) and, due to the element selectivity of core excitations, can be used as a local probe for the dynamics [54, 57–59]. SXRS measurements have been reported using XFEL pulses in atomic neon gas [60].

When two x-ray pulses interact with the sample, the resulting frequency-dispersed, two-pulse SXRS signal (FD2P-SXRS) depends on the single time-delay between the two pulses and the detected frequency. Integrating over the detected frequency gives the integrated two-pulse SXRS (I2P-SXRS) which can be Fourier transformed to give a 1D

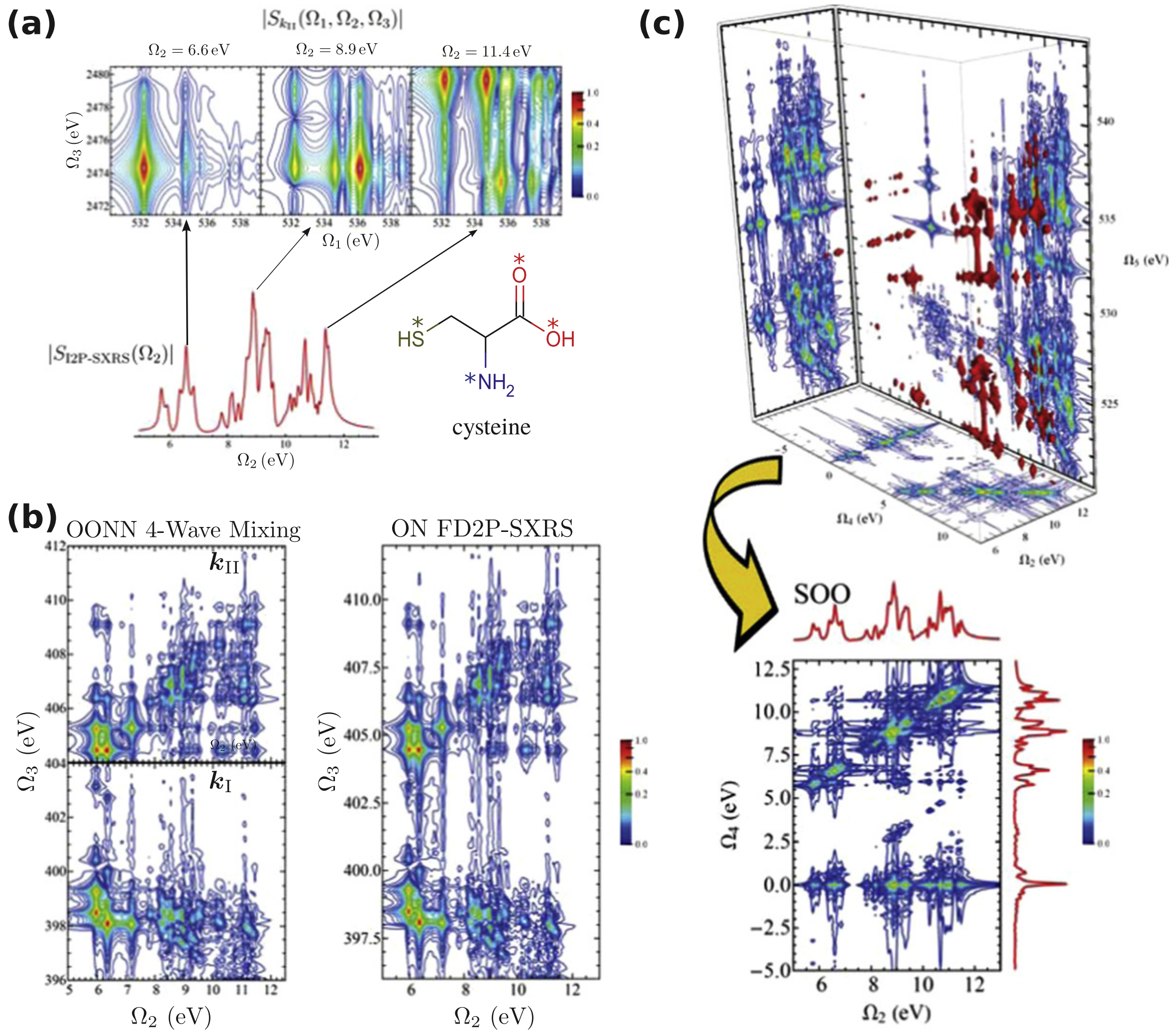

Figure 9. Calculated multidimensional SXRS signals reveal the coupling between various core and valence excitations localized at different x-ray chromorphores in cysteine (figure adapted with permission from [63]. Copyright AIP Publishing 2013.). (a) Projected FWM versus I2P-SXRS signals of cysteine. Different x-ray chromorphore centers in the molecule are labeled with stars of different colors. Constant-Ω_2 slice at the major SXRS peak positions of the 3D k_{II} signal using an OOSS sequence with *xxxx* polarization direction. The I2P-SXRS singal is for an OS pulse sequence and *xx* polarization direction. (b) Comparison of the FWM k_I and k_{II} signals (with the OONN pulse sequence and *xxxx* polarization) and the FD2P-SXRS signal (with an ON pulse sequence and *xx* polarization). (c) FD3P-SXRS signal and its 2D projection (I3P-SXRS) signal with an SOO pulse sequence and *xxx* polarization.

spectrum. This 1D spectrum is complementary to the 1D UV–vis absorption spectrum since some spectral lines may be inactive in absorption but Raman active (or vice versa).

By setting the interpulse delay time t_3 to zero, it is also possible to use 2P-SXRS as the probe in a pump-probe experiment. Such a probe has been utilized in femtosecond stimulated Raman spectroscopy (FSRS) to observe nonstationary states prepared by actinic pulses [61]. A classification scheme for different types of probes in pump-probe experiments was outlined in [62]. The zero-delay 2P-SXRS probe is then called ‘quadratic hybrid’ since it scales quadratically with probe-field intensity and the probe field consists of two pulses with different parameters (usually one broadband and one narrowband). The resultant signal then depends on the pump-probe delay and the probe parameters (in particular, the narrowband frequency). It can be frequency-dispersed or recorded in an integrated fashion.

Three-pulse experiments (3P-SXRS) can detect correlations between different electronic coherences. Interaction with the first pulse creates an electron–hole pair while the second interaction creates another electron–hole pair or alters the first. Either way, the two pairs must share a common electron or hole in order for the signal not to vanish.

3.1. Multidimensional stimulated x-ray Raman signals

Figure 9(a) connects the I2P-SXRS signal calculated for cysteine to the corresponding XFWM signal at $\mathbf{k}_{II} = \mathbf{k}_I - \mathbf{k}_2 + \mathbf{k}_3$. The time delay between the first and second pulse is now set to zero, so that the pump process is the same as that in an SXRS experiment. The $\mathbf{k}_{II}$ signal depends on two core excitation energies Ω_1, Ω_3 and a valence excitation energy Ω_2. The 3D $\mathbf{k}_{II}$ signal reveals a complex coupling pattern of the two core excitations and the valence excitation.

To interpret this signal, we set Ω_2 equal to the major valence excitations observed in the corresponding I2P-SXRS spectrum. In figure 9(a), we present the OS signals with pump at the oxygen K-edge and probe at the sulfur K-edge. By looking at the strong cross peaks in the projected 2D signals, one can easily understand how those core and valence excitations couple. For example, the 2474.2 eV S core excitation couples with the 532.2 eV O core excitation through the valence excitation 6.6 eV, as indicated by the leftmost 2D plot of figure 9(a). This strong coupling can be further rationalized by examining the relevant molecular orbitals (MOs) involved in these core and valence transitions. In short, with the help of I2P-SXRS, one can easily unravel the information about coupling of localized core and valence excitations hidden in the more complicated FWM signals.

Instead of collecting the integrated response of the probe pulse, it is also possible to record the dispersed spectrum of the probe pulse resulting in the FD2P-SXRS. In figure 9(b) we compare the XFWM signals $\mathbf{k}_{\mathrm{I}}$ and $\mathbf{k}_{\mathrm{II}}$ with the frequency dispersed two-pulse SXRS signals in the same energy range. One can see that they provide essentially the same information. SXRS is easier to implement since it does not require phase-matching between the pump and probe pulses, as required in XFWM. With an additional probe pulse, D2P-SXRS can be extended to three dimensions, yielding dispersed three-pulse SXRS (D3P-SXRS). This 3D signal reveals the coupling between valence excitations (Ω_2), valence excitations and deexcitations (Ω_4) and core excitations (Ω_5) (upper part of figure 9(c)). The projected 2D signals (lower part of figure 9(c)) represent the coupling pattern of valence excitations/deexcitations, under the impact of core excitations induced by the middle probe pulse. Comparing the 2D signals with different middle probe pulses would bring valuable insights on the complicated many-body interaction of localized excitations [63].

3.2. Monitoring excitation energy transfer in aggregates with SXRS

We now demonstrate the application of SXRS for studying excitation energy transfer (EET) in a model Zn-Ni porphyrin heterodimer. Porphyrin arrays are ubiquitous in natural and artificial light harvesting. The time-domain SXRS signal (equation (5)) can be viewed as the overlap of a time-dependent doorway state created by the pump pulse and a time-independent window state created by the probe pulse [64]. Two detecting modes are shown schematically in figure 10(a): the one-color signals for which the pump and probe are at the same edge and on the same porphyrin ring, and the two-color signal for which the pump and probe are not at the same edge and not on the same porphyrin ring. The time variation of these signals directly reflects the motion of the doorway wavepacket created by the pump pulse since the window wavepacket is static. The dominant natural orbitals of the time-dependent doorway wavepacket and the static window wavepacket are shown in figure 10(c). The back-and-forth oscillation between the two porphyrin rings can be clearly seen. This motion is reflected in the time-domain one-color (pump/probe at the Zn2p edge) and two-color (pump at the Zn2p edge/probe at the Ni2p edge) SXRS signals shown in the top panel of figure 10(b). The almost constant $\pi/2$ phase difference between the two signals illustrates this back-and-forth motion, as when the doorway and window wavepackets are at the same porphyrin ring, the one-color signal should reach its maximum but the two-color signal should be in minimum and vice versa.

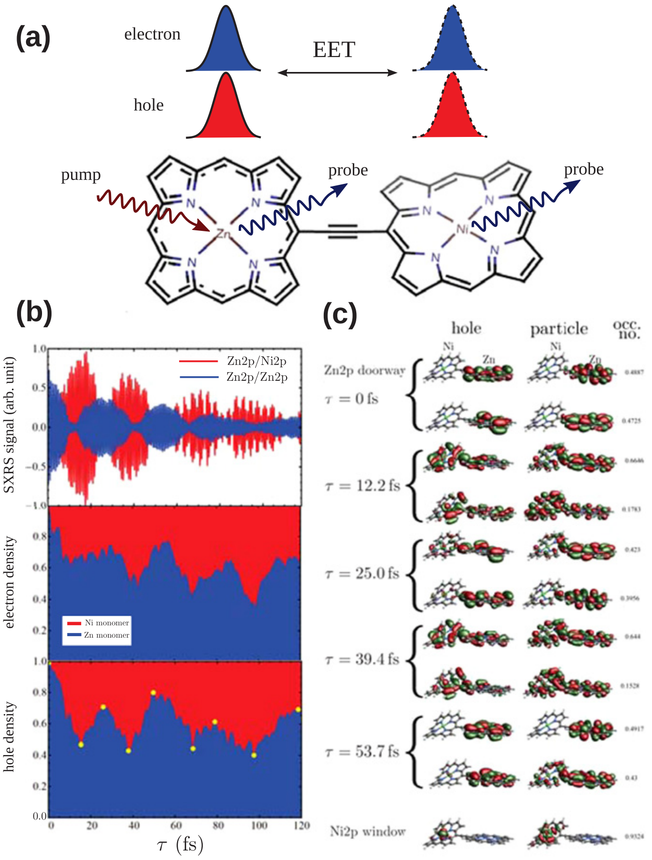

Figure 10. Time-domain SXRS signals reveal the excitation energy transfer dynamics in Zn-Ni porphyrin heterodimer (figure adapted with permission from [79]). Copyright PNAS 2013. (a) Schematic representation of electron and hole wavepackets moving back and forth between the Zn and Ni ring of the porphyrin dimer, denoting excitation energy transfer. The one-color (pump/probe at the same ring) and two-color (pump/probe at different rings) detecting modes are also shown. (b) Top: the time-domain integrated two-pulse SXRS signals of the porphyrin dimer between 0 and 120 fs. The one-color Zn2p/Zn2p (pump/probe at the Zn2p edge) signal is in blue and the two-color Zn2p/Ni2p (pump at the Zn2p edge and probe at the Ni2p edge) is in red. Middle and bottom: spatially integrated electron and hole densities on the Ni (in red) and Zn (in blue) ring. The yellow dots mark the local maxima and minima of the hole density fluctuation. (c) Dominant natural orbitals of the evolving Zn2p doorway wavepacket and the time-independent Ni2p window wavepacket.

We also calculated the time-dependent hole and electron densities of the valence excited state wavepacket prepared by the pump pulse on the two porphyrin rings. The two densities reach their maximum and minimum almost always simultaneously, which confirms that this is an excitation energy transfer, not an electron transfer process, and the two

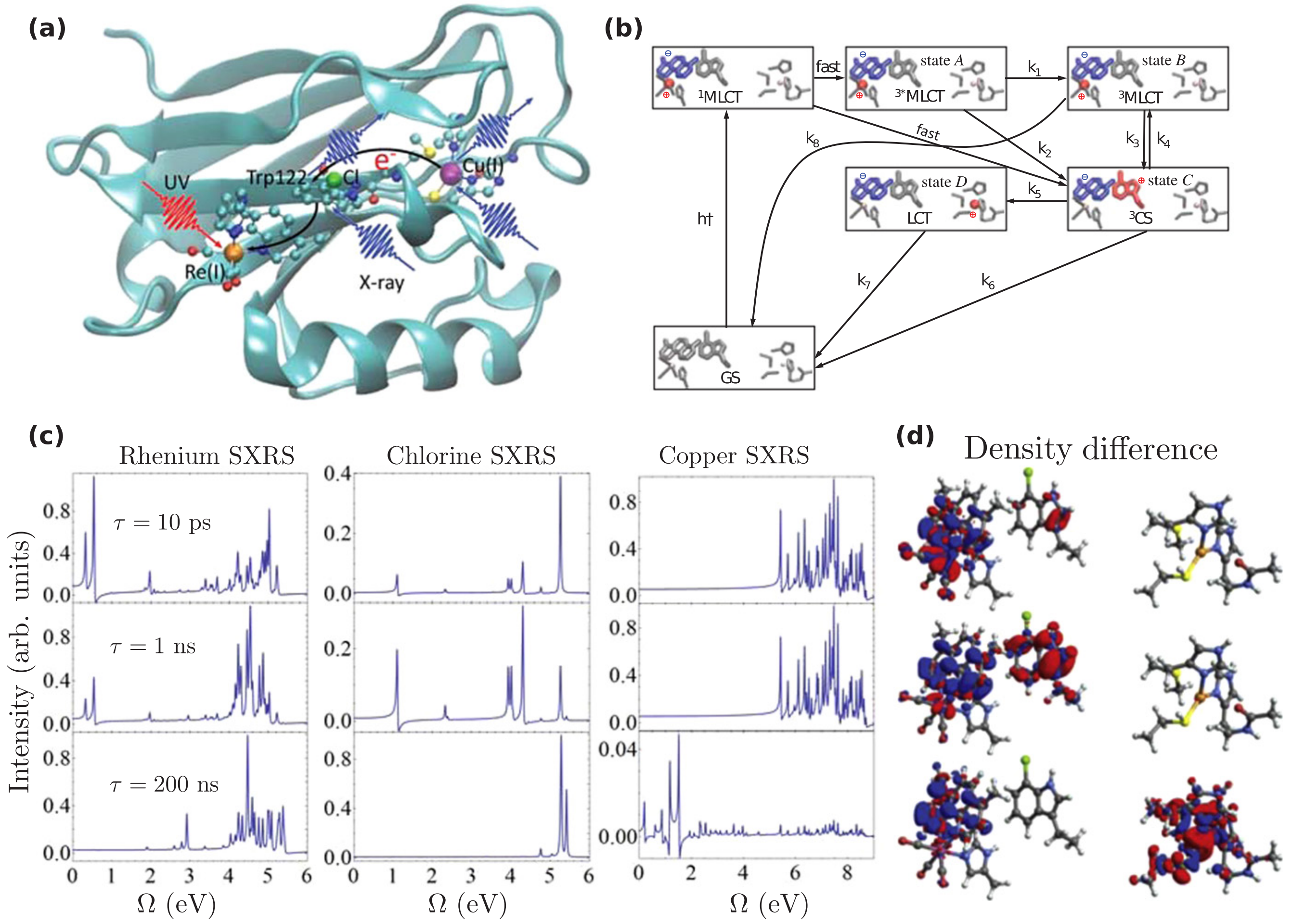

Figure 11. Time-resolved SXRS signals reveal the long-range electron transfer dynamics in azurin (figure adapted with permission from [65]. Copyright ACS Publications 2014.). (a) The electron transfer pathway from the Cu (I) center donor to Re (I) center acceptor via the Cl-substituted tryptophan intermediate. The excitation UV pulse and the probing x-ray pulses are also shown. (b) The electron transfer mechanism in this system. (c) One-color SXRS signals on the Re, Cl, and Cu K-edges at the delay time of 10 ps, 1 ns, and 200 ns, respectively. (d) Three snapshots of the electron density difference (excited state density minus ground state density) at the delay time of 10 ps, 1 ns, and 200 ns (from top to bottom, respectively). Hole density is represented by red and blue denotes electron density. Atomic color code: Re, pink; Cl, green; Cu, orange; N, blue; O, red; C, gray; H, white.

porphyrins remain neutral, as shown schematically in figure 10(a).

3.3. Monitoring electron transfer with SXRS

Long-range electron transfer (ET) is crucial in many energy conversion processes and biosynthetic reactions in living organisms. Understanding the detailed long-range ET pathways in biomolecular systems such as proteins may help the design of biomimetic catalysts and artificial light-harvesting devices. We consider the small protein azurin, in which a Re-complex is inserted which acts as the antenna to harvest the photon energy and trigger the long-range ET process. The ET pathway and possible detecting modes are shown schematically in figure 11(a). This is a two-step sequential electron hopping process, where the Cu-complex acts as the donor, the Re-complex is the acceptor, and a tryptophan residue acts as an intermediate bridge. The ET kinetics has been extensively studied by time-resolved IR and UV–vis spectroscopy [66] and the resulting kinetic model is shown in figure 11(b). Time-resolved IR and UV–vis do not directly detect the ET intermediate tryptophan and information about electron migrating to or leaving this intermediate can only by inferred from the changing spectroscopic features of the donor and the acceptor. In addition, IR and UV–vis features of the transient species involved in the long-range ET process heavily overlap, so that ET kinetic parameters must are obtained by global fitting techniques. As a complement to the existing IR and UV–vis techniques, SXRS gives distinct spectroscopic features of the intermediate species, thus the time-resolved SXRS signals become sensitive indicators of electron motion, as shown in figures 11(c) and (d). To selectively detect the tryptophan intermediate, we substitute it with a chlorine atom. This strategy is analogous to isotope labeling in IR spectroscopy. The SXRS signals at the donor, intermediate, and acceptor at three times during the ET process are shown in figure 11(c) and the corresponding electron density difference (transient state density minus ground state density) snapshots are presented in figure 11(d). The signals collected at the donor, intermediate, and acceptor give a complete picture of the electron flow path. The processes studied in figures 9–11 are not very fast and do not exploit the attosecond time resolution. However, they make use of the broadband excitation to detect many valence excitations. Faster ET processes could benefit from the high temporal resolution as well [67].

4. Linear and quadratic x-ray Raman probes

For temporally-well-separated pulses, SXRS can be viewed as a pump-probe technique in which an electronic coherence (or a superposition of such coherences) is created by one or several incoming pulses and is then probed in a Raman fashion by the final pulse. Generally speaking, when a pumping process (even a compound process comprised of multiple field–matter interactions) is well-separated in time from a subsequent probe, one can separate the pumping from the subsequent interpulse evolution and detection by the probe pulse. Since the type of information detectable in such a technique is entirely determined by the probing process, it is advantageous to classify pump-probe experiments by the nature of the probe. Such a systematic classification scheme was described in [62]. In particular, the signal may be defined as the frequency-dispersed transmission of the probe pulse (or one of the moments of this quantity), which may be shaped or hybrid broad-narrowband. Assuming Raman-type probing processes, such signals will have contributions that are linear, quadratic, and higher order in the probe-field intensity. Many common experiments can be analyzed from this perspective, allowing a comparison of the information available in various signals without specifying the pumping process in detail.

4.1. Probing conical intersections by TRUECARS

Let us reexamine the 2P-SXRS signal in the language of [62] (which is adequate for temporally well-separated pulses). In this picture, the first pulse pumps the molecule into a coherence ($\rho_{gg} \mapsto \rho_{g'g}$) via a Raman excitation and the second pulse probes this coherence after some delay time. We term this type of probing process 'linear broadband' since it is linear in the probe-field intensity and there is only a single probe-pulse with an assumed broad frequency band (as opposed to the hybrid probes discussed above) and the corresponding signal can again be recorded in a frequency-dispersed (FD) or integrated fashion. One may thus view an FD2P-SXRS experiment as a Raman pump followed by frequency-dispersed, linear detection of a probe. On resonance, the technique is known as transient absorption. In the off-resonant regime, such a signal consists solely of a parametric redistribution of photons in the probe pulse and does not have absorptive features. It therefore only probes electronic coherences; terms originating in electronic populations of the pumped system vanish. This frequency-dispersed linear off-resonant probe technique is therefore a background-free measurement of the effects of electronic coherence in the system (see figure 12).

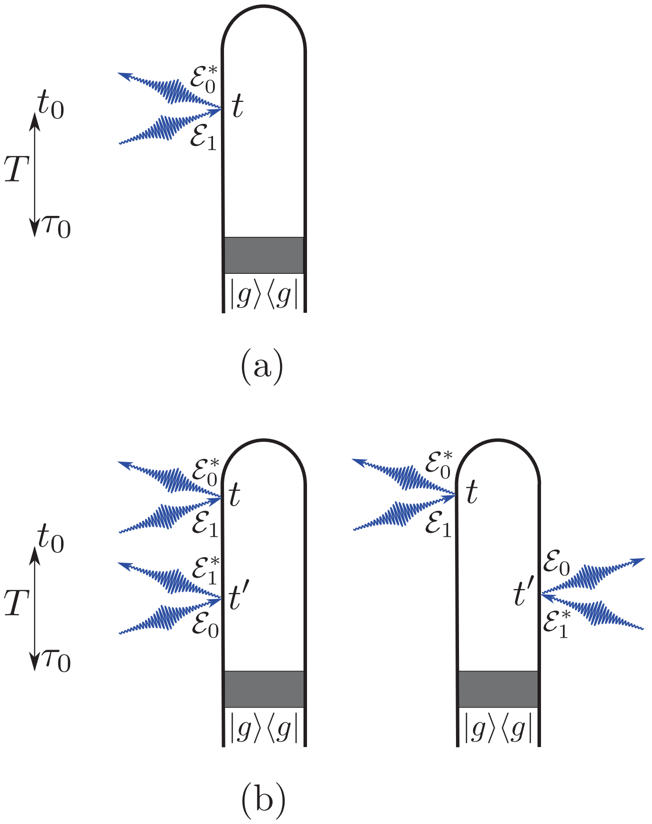

Figure 12. Diagrams corresponding to linear TRUECARS (a) and quadratic ASRS (b) detection of nonstationary states in pump-probe experiments. In all diagrams, the shaded rectangle represents an unspecified pumping process that terminates by some well-defined time. The system then evolves freely before interacting with the probing pulse which can be broadband ($\mathbf{E}_0 = \mathbf{E}_1$) or hybrid ($\mathbf{E}_0 \neq \mathbf{E}_1$ with $\mathbf{E}_j$ the field envelope of probing field j). In these signals, the phases of each pulse cancel due to the two interactions and the wavevector-based phase-matching is no longer necessary to observe the signal. We therefore label the interactions by their field amplitudes, the profiles of which determine the signal.

In the off-resonant FD2P-SXRS technique, a Raman excitation creates a coherence which is then tracked via a frequency-dispersed linear off-resonant probe. In the absence of this externally-generated electronic coherence, the signal vanishes as described above. A similar technique is possible in which the pumping process is an actinic pump to an electronic excited state rather than a coherence. For short pump-probe delay times, this signal vanishes since it contains no coherences. However, non-adiabatic coupling between the electronic states can generate electronic coherences in the course of the material propagation. One thus observes oscillations due to the internally created electronic coherences and the signal no longer vanishes. We term this technique 'transient redistribution of ultrafast electronic coherences by attosecond Raman spectroscopy' or TRUECARS [68]. Energy is redistributed between the red and blue components of the pulse spectrum but there is no net absorption of photons.

In figure 13, we show the TRUECARS signal simulated for a model system in which a vibrational wavepacket is

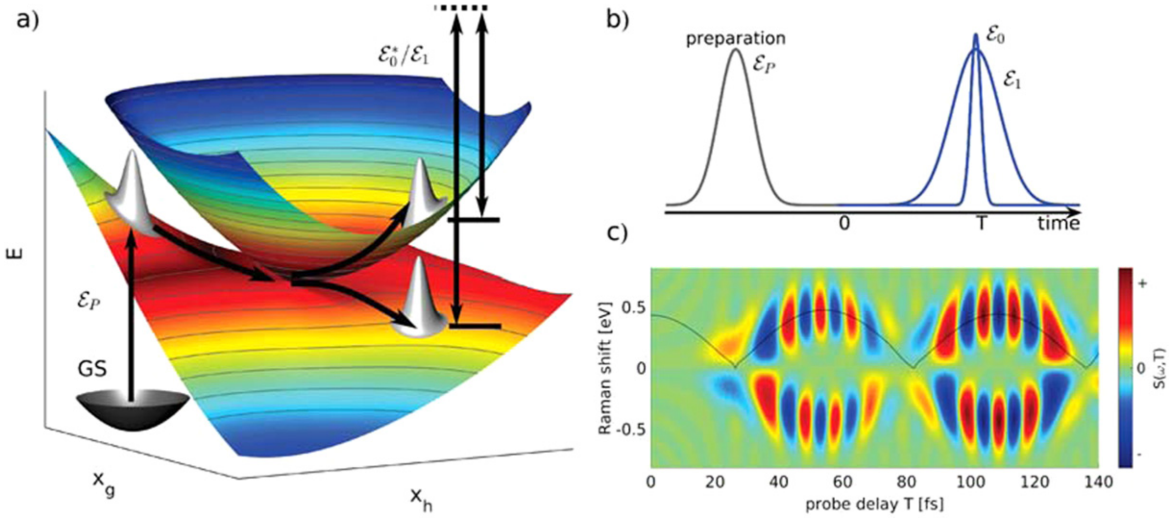

Figure 13. The TRUECARS signal. (a) A nuclear wave packet is promoted from the ground state (GS) by a pump-pulse $\mathcal{E}_P$ to an excited electronic state. As it passes the coupling region around the CoIn, a coherence is created between the two electronic states. The broadband $\mathcal{E}_0$/narrowband $\mathcal{E}_1$ hybrid pulse probes the electronic coherence between the nuclear wave packets on different surfaces. (b) Schematics of the pump and hybrid-probe pulse sequence. (c) The signal calculated for a model system with two electronic states and a single vibrational coordinate. The energy splitting of the electronic states involved in the coherence (solid line) can be read from the Raman shift and the coherent oscillation period reveals this time-dependent splitting averaged over the nuclear wavepacket. Adapted with permission from [68]. Copyright American Physical Society 2015.

prepared on an electronic excited state potential energy surface and propagates toward a conical intersection (CoIn) where the Born–Oppenheimer approximation (the separation of electronic and nuclear motions), or BOA, breaks down. As the system approaches the CoIn and becomes subject to nonadiabatic coupling, population leaks to the other surface, generating coherences in the process. Coherent oscillations are then observed in the TRUECARS signal with a period corresponding to the separation between electronic potential surfaces (spatially averaged over the nuclear wavepacket). Spectrally, one can see the separation between the two electronic excited surfaces evolving with time. The large cross-section for such a Raman redistribution process compared to photoionization has been recently estimated [69].

4.2. Attosecond x-ray Raman spectroscopy

It is possible to use a zero-delay two-pulse SXRS process as a probe in a pump-probe experiment (see figure 12(b)). Such a hybrid probe comprised of, e.g. broadband and narrowband components, offers unique advantages over simpler probe fields. Pump-probe style experiments have been conducted in the femtosecond regime in which an actinic pump pulse populates electronic excited states the dynamics of which is then probed by a hybrid broad-narrow pulse and the signal is given by the frequency-dispersed transmission of the broadband component of the probe pulse. Such experiments termed femtosecond stimulated Raman spectroscopy offer advantages over the simpler transient absorption experiments. In FSRS, the narrowband component of the hybrid probe gives sharp peaks at the Raman resonances while the broadband component (narrowly-confined in time) provides high temporal resolution for the probing process. In this way, the temporal and spectral resolutions of the resultant spectra are not connected by a Fourier uncertainty relation and more well-defined features are accessible compared to a transient absorption experiment with a broadband probe. These hybrid probe pulses also inspire a broader class of pump-probe experiments in which the probe pulse can be shaped and tailored to various specifications.

Using a hybrid broad-narrowband probe to track the population dynamics of excited states in the attosecond regime gives attosecond stimulated Raman spectroscopy (ASRS) [56]. Core-level electron excitations from different atoms are generally well-separated spectrally. Thus, ASRS can probe dynamical changes locally near specific atoms in complex molecules. This can be used to monitor femtosecond charge and excitation energy transfer processes [9, 65] and passage through CoIns in photo-induced chemical reactions [42]. The ASRS signal is a quadratic-probe signal [62] and is therefore of a higher order in probe–matter interaction than TRUECARS and scales differently with probe intensity (quadratically versus linearly), thus allowing their separation.

5. Discussion and summary

Advancements in x-ray light sources have enabled new nonlinear spectroscopic tools that reveal core-level electronic resonances and their interactions, and permit the creation of nonstationary electronic wavepackets of valence excitations and monitoring their dynamics. At these frequencies and timescales, experimental techniques are generally sensitive to electronic coherences as well as populations. SXRS exploits the broad bandwidth of x-ray pulses to create nonstationary superpositions of electronic coherences at well-defined times.

These are subsequently monitored, giving a window into the electronic and nuclear dynamics as well as the coupling between various core and valence level excitations. This technique can thus reveal charge and excitation energy transfer in complex systems. The role of electronic coherence in many such naturally occurring processes is not well understood. For example, an open question is to what extent quantum coherence effects are responsible for the efficiency of light-harvesting complexes [70]. The tracking of electronic coherences made possible by the extension of nonlinear spectroscopic techniques to the x-ray regime will be most valuable in answering these questions.

With the high (femtosecond–attosecond) time-resolution afforded by x-ray pulses, ultrafast dynamics of populations can be studied. We have shown how, for example, dynamics can be launched via excitation to an electronic excited state with an actinic pump and then subsequently tracked using a linear probe (TRUECARS) or a quadratic probe (ASRS). These techniques can track the evolution of time-dependent energy gaps between states. The attosecond time-resolution is particularly useful for tracking evolution through a CoIn between excited states. As is well known, CoIns facilitate ultrafast population transport between electronic states and are therefore hard to resolve with longer pulses. CoIns provide a fast non-radiative decay pathway that controls product yields and rates in virtually all photophysical and photochemical processes. Their ubiquity and nontrivial physics (both with respect to transient, ultrafast phenomena, and multiple intercoupled excited states) make CoIns ideal candidates for nonlinear x-ray spectroscopy. Techniques such as TRUECARS offer a means of observing the electronic coherences generated by the non-BOA coupling characteristic of CoIns.

Here, we have surveyed various possible applications of nonlinear x-ray spectroscopy techniques (FWM, 1D- and 2D-SXRS, ASRS, and TRUECARS). We showed how nonlinear x-ray spectroscopies can track ultrafast passage through conical intersections and reveal the time evolution and couplings of electronic coherences. More elaborate pulse sequences could map the potential energy surfaces with particular focus to the region around a CoIn. Moreover, this could naturally provide a platform to address the role of geometric (Berry) phase effects in molecular dynamics near CoIns. Future investigations could include incoherent detection of the coherent effects induced by pulse sequences described above through fluorescence, currents, and photoelectron or Auger electron emissions. These incoherent detection modes are more versatile and often more convenient [71]. Electron spectroscopies, including time-resolved photoelectron spectroscopy (TRPES) and Auger probing following x-ray pulse sequences should be extremely valuable [72–74, 78]. Electron rather than photon detection is more sensitive in many cases. Auger transitions depend on different selection rules compared to those for dipolar transitions and so probing Auger electrons will be complementary to other nonlinear spectroscopic techniques. It is also possible to photoionize a system using shaped pulses as in the hybrid probes considered above for Raman techniques. For example, the streak camera and RABBIT (reconstruction of attosecond beating by interference of two-photon transitions) techniques use a combination IR-XUV field (the former uses a few-cycle IR field and single attosecond XUV pulse while the latter utilizes a CW IR laser and an attosecond pulse train) to perform pulse characterization and high-resolution fast photoelectron detection [75–77]. Combined with the variety of photon detection based nonlinear x-ray spectroscopies (some of which we discussed above), these electron spectroscopies will help build a toolbox of possible experiments that can be employed in various scenarios and parameter regimes to shed light on previously-inaccessible dynamics and energy regimes, dramatically improving our understanding of molecular processes.

Acknowledgments

The support of the Chemical Sciences, Geosciences, and Biosciences division, Office of Basic Energy Sciences, Office of Science, US Department of Energy through award No. DE-FG02-04ER15571 as well as from the National Science Foundation (grant CHE-1361516) and the Freiburg Institute for Advanced Studies (FRIAS) is gratefully acknowledged. The computational resources and the support for KB was provided by DOE. MK gratefully acknowledges support from the Alexander von Humboldt Foundation through the Feodor Lynen program.

References

[1] Barty A *et al* 2008 Ultrafast single-shot diffraction imaging of nanoscale dynamics *Nat. Photon.* **2** 415–9

[2] Seibert M M *et al* 2011 Single mimivirus particles intercepted and imaged with an x-ray laser *Nature* **470** 78–81

[3] Richard R, Ernst G B and Wokaun A 1990 *Principles of Nuclear Magnetic Resonance in One and Two Dimensions* (Oxford: Clarendon)

[4] Mukamel S and Bakker H J 2015 Special topic on multidimensional spectroscopy *J. Chem. Phys.* **142** 212101

[5] Mukamel S 1995 *Principles of Nonlinear Optical Spectroscopy* (New York: Oxford University Press)

[6] Friebolin H 2010 *Basic One- and Two-Dimensional NMR Spectroscopy* 5th edition (Weinheim: Wiley)

[7] Rule G S and Hitchens T K 2006 *Fundamentals of Protein NMR Spectroscopy* (Amsterdam: Springer)

[8] Scheurer C and Mukamel S 2002 Magnetic resonance analogies in multidimensional vibrational spectroscopy *Bull. Chem. Soc. Jpn.* **75** 989–99

[9] Zhang Y, Biggs J D, Hua W, Dorfman K E and Mukamel S 2014 Three-dimensional attosecond resonant stimulated x-ray raman spectroscopy of electronic excitations in core-ionized glycine *Phys. Chem. Chem. Phys.* **16** 24323–31

[10] Tanimura Y and Mukamel S 1993 Two-dimensional femtosecond vibrational spectroscopy of liquids *J. Chem. Phys.* **99** 9496–511

[11] Savolainen J, Ahmed S and Hamm P 2013 Two-dimensional Raman-terahertz spectroscopy of water *Proc. Natl. Acad. Sci. USA* **110** 20402–7

[12] Patterson B D 2010 *SLAC-TN-10-026 Resource Letter on Stimulated Inelastic X-ray Scattering at an XFEL* Technical Note (http://slac.stanford.edu/pubs/slactns/tn04/slac-tn-10-026.pdf)

[13] West B A, Womick J M and Moran A M 2011 Probing ultrafast dynamics in adenine with mid-UV four-wave mixing spectroscopies *J. Phys. Chem.* A **115** 8630–7

[14] Allaria E *et al* 2013 Two-colour pump-probe experiments with a twin-pulse-seed extreme ultraviolet free-electron laser *Nat. Commun.* **4** 2476

[15] Mukamel S, Healion D, Zhang Y and Biggs J D 2013 Multidimensional attosecond resonant x-ray spectroscopy of molecules: lessons from the optical regime *Annu. Rev. Phys. Chem.* **64** 101–27

[16] Balzani V, Ceroni P and Juris A 2014 *Photochemistry and Photophysics: Concepts, Research, Applications* (Weinheim: Wiley)

[17] Corkum P B and Krausz F 2007 Attosecond science *Nat. Phys.* **3** 381–7

[18] Corkum P B 2013 *Attosecond Physics: Attosecond Measurements and Control of Physical Systems* (Berlin: Springer) pp 3–7

[19] Popmintchev T *et al* 2012 Bright coherent ultrahigh harmonics in the keV x-ray regime from mid-infrared femtosecond lasers *Science* **336** 1287–91

[20] Chen M-C *et al* 2014 Generation of bright isolated attosecond soft x-ray pulses driven by multicycle midinfrared lasers *Proc. Natl Acad. Sci. USA* **111** E2361–7

[21] Chen M-C *et al* 2015 Bright isolated attosecond soft x-ray pulses *Ultrafast Phenomena XIX* (Berlin: Springer) 95–8

[22] Khalil M, Demirdöven N and Tokmakoff A 2003 Obtaining absorptive line shapes in two-dimensional infrared vibrational correlation spectra *Phys. Rev. Lett.* **90** 047401

[23] Tian P, Keusters D, Suzaki Y and Warren W S 2003 Femtosecond phase-coherent two-dimensional spectroscopy *Science* **300** 1553–5

[24] Tanaka S and Mukamel S 2002 X-ray four-wave mixing in molecules *J. Chem. Phys.* **116** 1877–91

[25] Tanaka S and Mukamel S 2003 Probing exciton dynamics using raman resonances in femtosecond x-ray four-wave mixing *Phys. Rev.* A **67** 033818

[26] Mukamel S 2005 Multiple core-hole coherence in x-ray four-wave-mixing spectroscopies *Phys. Rev.* B **72** 235110

[27] Zhang Y, Healion D, Biggs J D and Mukamel S 2013 Double-core excitations in formamide can be probed by x-ray double-quantum-coherence spectroscopy *J. Chem. Phys.* **138** 144301

[28] Mukamel S and Rahav S 2010 *Ultrafast Nonlinear Optical Signals Viewed from the Molecules Perspective: Kramers-Heisenberg Transition Amplitudes versus Susceptibilities* (*Advances in atomic, Molecular, and Optical Physics* vol. 59) ed P Berman *et al* (Amsterdam: Elsevier) 223–263 ch 6

[29] Kim J, Mukamel S and Scholes G D 2009 Two-dimensional electronic double-quantum coherence spectroscopy *Acc. Chem. Res.* **42** 1375–84

[30] Schweigert I V and Mukamel S 2008 Double-quantum-coherence attosecond x-ray spectroscopy of spatially separated, spectrally overlapping core-electron transitions *Phys. Rev.* A **78** 052509

[31] Abramavicius D, Palmieri B, Voronine D V, Šanda F and Mukamel S 2009 Coherent multidimensional optical spectroscopy of excitons in molecular aggregates; quasiparticle versus supermolecule perspectives *Chem. Rev.* **109** 2350–408

[32] Zhang Y, Healion D, Biggs J D and Mukamel S 2013 Double-core excitations in formamide can be probed by x-ray double-quantum-coherence spectroscopy *J. Chem. Phys.* **138** 144301–14

[33] Hua W, Bennett K, Zhang Y, Luo Y and Mukamel S 2016 Study of double core hole excitations in molecules by X-ray double-quantum-coherence signals: a multi-configuration simulation *Chem. Sci.* (doi:10.1039/C6SC01571A)

[34] Malmqvist P, Rendell A and Roos B O 1990 The restricted active space self-consistent-field method, implemented with a split graph unitary group approach *J. Phys. Chem.* **94** 5477–82

[35] Zhang Y, Hua W, Bennett K and Mukamel S 2016 Nonlinear spectroscopy of core and valence excitations using short x-ray pulses: simulation challenges *Density-Functional Methods for Excited States* (*Topics in Current Chemistry* 368) ed N Ferré *et al* (Berlin: Springer) 273–345

[36] Jensen H J, Jørgensen P and Ågren H 1987 Efficient optimization of large scale MCSCF wave functions with a restricted step algorithm *J. Chem. Phys.* **87** 451–66

[37] Ågren H and Jensen H J Å 1987 An efficient method for the calculation of generalized overlap amplitudes for core photoelectron shake-up spectra *Chem. Phys. Lett.* **137** 431–6

[38] Ågren H, Flores-Riveros A and Jensen H J Å 1989 An efficient method for calculating molecular radiative intensities in the VUV and soft x-ray wavelength regions *Phys. Scr.* **40** 745

[39] Ågren H and Jensen H J Å 1993 Relaxation and correlation contributions to molecular double core ionization energies *Chem. Phys.* **172** 45–57

[40] Tashiro M, Ehara M, Fukuzawa H, Ueda K, Buth C, Kryzhevoi N V and Cederbaum L S 2010 Molecular double core hole electron spectroscopy for chemical analysis *J. Chem. Phys.* **132** 184302

[41] Josefsson I, Kunnus K, Schreck S, Föhlisch A, de Groot F, Wernet P and Odelius M 2012 *Ab initio* calculations of x-ray spectra: atomic multiplet and molecular orbital effects in a multiconfigurational SCF approach to the l-edge spectra of transition metal complexes *J. Phys. Chem. Lett.* **3** 3565–70

[42] Hua W, Oesterling S, Biggs J D, Zhang Y, Ando H, de Vivie-Riedle R, Fingerhut B P and Mukamel S 2016 Monitoring conical intersections in the ring opening of furan by attosecond stimulated x-ray Raman spectroscopy *Struct. Dyn.* **3** 023601

[43] Cho M J, Choi D H, Sullivan P A, Akelaitis A J P and Dalton L R 2008 Recent progress in second-order nonlinear optical polymers and dendrimers *Prog. Polym. Sci.* **33** 1013–58

[44] Suhr Kirketerp M-B, Åxman Petersen M, Wanko M, Andres L, Leal E, Zettergren H, Raymo F M, Rubio A, Brøndsted Nielsen M and Brøndsted Nielsen S 2009 Absorption spectra of 4-nitrophenolate ions measured in vacuo and in solution *ChemPhysChem* **10** 1207–9

[45] Wanko M, Houmøller J, Støchkel K, Suhr Kirketerp M-B, Åxman Petersen M, Nielsen M B, Nielsen S B and Rubio A 2012 Substitution effects on the absorption spectra of nitrophenolate isomers *Phys. Chem. Chem. Phys.* **14** 12905–11

[46] Thomas A G, Jackman M J, Wagstaffe M, Radtke H, Syres K, Adell J, Lévy A and Martsinovich N 2014 Adsorption studies of p-aminobenzoic acid on the anatase TiO_2(101) surface *Langmuir* **30** 12306–14

[47] Fingerhut B P, Bennett K, Roslyak O and Mukamel S 2013 Selective assignment of energy transfer and charge separation pathways in reaction centers by pulse polarized 2D photon echo spectroscopy *EPJ Web of Conferences* **41** 07014

[48] Schweigert I V and Mukamel S 2007 Coherent ultrafast core-hole correlation spectroscopy: x-ray analogues of multidimensional NMR *Phys. Rev. Lett.* **99** 163001

[49] Schweigert I V and Mukamel S 2008 Probing interactions between core-electron transitions by ultrafast two-dimensional x-ray coherent correlation spectroscopy *J. Chem. Phys.* **128** 184307

[50] Healion D M, Schweigert I V and Mukamel S 2008 Probing multiple core-hole interactions in the nitrogen K-edge of DNA base pairs by multidimensional attosecond x-ray

spectroscopy a simulation study *J. Phys. Chem.* A **112** 11449–61

[51] Mukamel S, Abramavicius D, Yang L, Zhuang W, Schweigert I V and Voronine D V 2009 Coherent multidimensional optical probes for electron correlations and exciton dynamics: from NMR to x-rays *Acc. Chem. Res.* **42** 553–62

[52] Noziés P and de Dominicis C T 1969 Singularities in the x-ray absorption and emission of metals: III. One-body theory exact solution *Phys. Rev.* **178** 1097–107

[53] Schwarz W H E and Buenker R J 1976 Use of the Z+1-core analogy model: examples from the core-excitation spectra of CO_2 and N_2O *Chem. Phys.* **13** 153–60

[54] Schweigert I V and Mukamel S 2007 Probing valence electronic wave-packet dynamics by all x-ray stimulated Raman spectroscopy: a simulation study *Phys. Rev.* A **76** 012504

[55] Biggs J D, Zhang Y, Healion D and Mukamel S 2013 Multidimensional x-ray spectroscopy of valence and core excitations in cysteine *J. Chem. Phys.* **138** 144303

[56] Healion D, Zhang Y, Biggs J D, Govind N and Mukamel S 2012 Entangled valence electron–hole dynamics revealed by stimulated attosecond x-ray Raman scattering *J. Phys. Chem. Lett.* **3** 2326–31

[57] Tanaka S and Mukamel S 2002 Coherent x-ray Raman spectroscopy: a nonlinear local probe for electronic excitations *Phys. Rev. Lett.* **89** 043001

[58] Tanaka S, Volkov S and Mukamel S 2003 Time-resolved x-ray Raman spectroscopy of photoexcited polydiacetylene oligomer: a simulation study *J. Chem. Phys.* **118** 3065–77

[59] Mukamel S and Wang H 2010 Manipulating quantum entanglement of quasiparticles in many-electron systems by attosecond x-ray pulses *Phys. Rev.* A **81** 062334

[60] Weninger C, Purvis M, Ryan D, London R A, Bozek J D, Bostedt C, Graf A, Brown G, Rocca J J and Rohringer N 2013 Stimulated electronic x-ray Raman scattering *Phys. Rev. Lett.* **111** 233902

[61] Dorfman K E, Fingerhut B P and Mukamel S 2013 Time-resolved broadband Raman spectroscopies: a unified six-wave-mixing representation *J. Chem. Phys.* **139** 124113

[62] Dorfman K E, Bennett K and Mukamel S 2015 Detecting electronic coherence by multidimensional broadband stimulated x-ray Raman signals *Phys. Rev.* A **92** 023826

[63] Biggs J D, Zhang Y, Healion D and Mukamel S 2013 Multidimensional x-ray spectroscopy of valence and core excitations in cysteine *J. Chem. Phys.* **138** 144303

[64] Yan Y J and Mukamel S 1990 Femtosecond pump-probe spectroscopy of polyatomic molecules in condensed phases *Phys. Rev.* A **41** 6485–504

[65] Zhang Y, Biggs J D, Govind N and Mukamel S 2014 Monitoring long-range electron transfer pathways in proteins by stimulated attosecond broadband x-ray Raman spectroscopy *J. Phys. Chem. Lett.* **5** 3656–61

[66] Shih C *et al* 2008 Tryptophan-accelerated electron flow through proteins *Science* **320** 1760–2

[67] Zidek K, Zheng K, Ponseca C S Jr, Messing M E, Wallenberg L R, Chábera P, Abdellah M, Sundstrom V and Pullerits T 2012 Electron transfer in quantum-dot-sensitized ZnO nanowires: ultrafast time-resolved absorption and terahertz study *J. Am. Chem. Soc.* **134** 12110–7

[68] Kowalewski M, Bennett K, Dorfman K E and Mukamel S 2015 Catching conical intersections in the act: monitoring transient electronic coherences by attosecond stimulated x-ray Raman signals *Phys. Rev. Lett.* **115** 193003

[69] Miyabe S and Bucksbaum P 2015 Transient impulsive electronic Raman redistribution *Phys. Rev. Lett.* **114** 143005

[70] Cheng Y-C and Fleming G R 2009 Dynamics of light harvesting in photosynthesis *Annu. Rev. Phys. Chem.* **60** 241–62

[71] Agarwalla B K, Harbola U, Hua W, Zhang Y and Mukamel S 2015 Coherent (photon) versus incoherent (current) detection of multidimensional optical signals from single molecules in open junctions *J. Chem. Phys.* **142** 212445

[72] McFarland B K *et al* 2014 Ultrafast x-ray Auger probing of photoexcited molecular dynamics *Nat. Commun.* **5** 4235

[73] Moulet A, Bertrand J B, Jain A, Garg M, Luu T T, Guggenmos A, Pabst S, Krausz F and Goulielmakis E 2014 Attosecond pump-probe measurement of an Auger decay *Int. Conf. on Ultrafast Phenomena* 10 pages -Thu. Optical Society of America

[74] Bennett K, Kowalewski M and Mukamel S 2015 Probing electronic and vibrational dynamics in molecules by time-resolved photoelectron, Auger-electron, and x-ray photon scattering spectroscopy *Faraday Discuss.* **177** 405–28

[75] Krausz F and Ivanov M 2009 Attosecond physics *Rev. Mod. Phys.* **81** 163

[76] Kim K T, Zhang C, Shiner A D, Kirkwood S E, Frumker E, Gariepy G, Naumov A, Villeneuve D M and Corkum P B 2013 Manipulation of quantum paths for space–time characterization of attosecond pulses *Nat. Phys.* **9** 159–63

[77] Dahlström J M, L'Huillier A and Maquet A 2012 Introduction to attosecond delays in photoionization *J. Phys. B: At., Mol. Opt. Phys.* **45** 183001

[78] Bennett K, Kowalewski M and Mukamel S 2016 Nonadiabatic dynamics may be probed through electronic coherence in time-resolved photoelectron spectroscopy *J. Chem. Theory Comput.* **12** 740–52

[79] Biggs J D, Zhang Y, Healion D and Mukamel S 2013 *Proc. Natl Acad. Sci. USA* **110** 15597–601